


Article

Low-Frequency Sea Surface Radar Doppler Echo

Yury Yu. Yurovsky ^{1,2*} , Vladimir N. Kudryavtsev ^{1,2}, Semyon A. Grodsky ³ and Bertrand Chapron ^{2,4}

¹ Marine Hydrophysical Institute Russian Academy Sci., 2 Kapitanskaya, Sevastopol, Russia; yyyurovsky@gmail.com

² Russian State Hydrometeorological University, 98 Malookhotinskiy, St-Petersburg, Russia; kudr@rshu.ru

³ University of Maryland, College Park, MD, USA; senya@umd.edu

⁴ Institut Français de Recherche pour l'Exploitation de la Mer, 29280, Plouzané, France; bertrand.chapron@ifremer.fr

* Correspondence: yyyurovsky@gmail.com; Tel.: +7-978-789-11-31

Abstract: Observed sea surface Ka-band normalized radar backscatter cross section (NRCS) and Doppler velocity (DV) exhibit energy at low frequencies (LF) below the surface wave range. It is shown that non-linearity in NRCS-wave slope Modulation Transfer Function (MTF) and inherent NRCS averaging within the footprint account for the NRCS and DV LF variance with the exception of VV NRCS for which almost half of the LF variance is attributable to wind fluctuations. Although the distribution of radar DV is quasi-Gaussian suggesting virtually little impact of non-linearity, the LF DV variations arise due to footprint averaging of correlated local DV and non-linear NRCS. Numerical simulations demonstrate that MTF non-linearity weakly affects traditional linear MTF estimate (less than 10% for $|MTF| < 20$). Thus the linear MTF is a good approximation to evaluate the DV averaged over large footprints typical of satellite observations.

Keywords: Radar; ocean; backscatter; Doppler shift; wave groups; non-linearity; modulation

1. Introduction

Doppler frequency shift of radar backscattering from the sea surface and corresponding Doppler Velocity (DV) are governed by the surface kinematics. In early studies, the DV measured by a coherent radar was used as a proxy for wave gauge (WG) to examine wave-induced modulations of the normalized radar cross-section (NRCS) [1–3]. Further, along-track interferometry [4–6] as well as Doppler centroid anomaly [7–9] methods were used to demonstrate an ability to detect surface currents from air/space-borne radar platforms. Recently, the DV has been explored as a key parameter for future satellite ocean current missions based on the Doppler rotating beam scatterometry [10–14].

Surface waves modulate local DV and NRCS and thus produce a wave-induced mean component of the DV due to correlated modulations of DV and NRCS, which doesn't zero after averaging over long wave scales. The wave-induced DV is not small [6,9,15,16] and is important for retrieving surface currents from measured DV.

Besides variation in the frequency range of surface waves, the DV and NRCS reveal a low-frequency variation (LF) at sub-wave frequencies. Plant et al. [17] have found that LF NRCS spectral density is comparable in size to wave-induced spectral density. It is larger for L-band than for X-band and depends on wind. From these observations it has been concluded that LF NRCS variations are not a system-related noise, but produced by turbulent wind fluctuations on sub-wave frequencies, which are uncorrelated with surface waves. Alternatively, Grodsky et al. [18] have attributed LF NRCS variations to wave groups (assuming constant wind).

The presence of X-band LF DV variations has been reported in [17,19]. Such variations are especially large at HH polarization and increase with incidence angle (see Fig. 5 in [19]). Numerical simulations of Plant [19] have shown that LF DV variations can be explained by fast scatterers associated with the bound (parasitic) waves. Interestingly, at low grazing angles, Hwang et al. [20]

have found that radar-derived wave periods are longer by about 20–27% than those measured by nearby buoy and explained this by wave breaking spikes present not on every dominant wave crest. Given that breaking waves are related to wave groups [21], this mechanism is somewhat similar to that proposed in [18].

If coherent for DV and NRCS [17], such LF variations may produce an additional time-mean DV component after averaging over their time/space scales. Particularly, a real aperture Doppler scatterometer with a few kilometer footprint inherently averages a product of LF DV and NRCS variations. Besides wind-induced variations, the correlated LF variations of NRCS and DV may originate from impacts of wave groups (via wave breaking and Stokes drift), oil slicks, Langmuir circulations (via Bragg wave damping), small-scale current eddies, etc. Thus, the understanding of nature of LF radar variations is important for accessing their impact on the time mean DV.

The origin of LF fluctuations is examined using Ka-band platform-based measurements [22,23] that include well pronounced LF features. We focus on explanations of observed NRCS and DV spectra, and their cross-spectrum, which define the time mean LF DV contribution. The analysis is based on radar measurements and their comparison with concurrent wind and wave measurements. Using a primitive numerical backscattering simulation, we demonstrate how the impact of LF variations can be explained.

2. Experiment

The measurements were carried out in the Black sea from a static research platform located 600 m offshore in a 30 m deep water. A Ka-band (37.5 GHz) dual-copolarized (VV and HH) continuous wave Doppler radar was used to obtain time series of the sea surface NRCS and DV (details on the radar calibration and measurement techniques are given in [22,23]). Simultaneous wave measurements were performed using a resistant wire wave gauge (WG) operated at 20 Hz sampling rate. Wind velocity was measured at 0.2 Hz sampling rate by a vane anemometer installed at 21 m height on platform mast.

We select a typical one hour sample record that includes LF features. The radar was installed at 12 m height at $\theta = 48^\circ$ incidence angle and directed upwind (wind and dominant waves both coming from the east). For this observation geometry, the radar surface footprint was about 2 m in width and 4 m in length.

On the measurement day (12-Sep-2012, Fig. 1), the wind speed accelerated at about 04:00 UTC reaching maximum of about 15 m/s by 05:00 UTC. Wave development lagged the wind amplification and then they calmed down after 18:00 UTC. The measurements, we consider, were taken between 13:20 UTC and 14:20 UTC when wind waves became steady and no strong swell present. During the acquisition period, the mean wind speed was 6 m/s with 0.7 m significant wave height. The wind wave spectrum (see Fig. 3a below) was close to the saturation level for wave frequency > 0.38 Hz (to within the Toba empirical confidence range [24]) but had somewhat weaker spectral level between 0.19 Hz and 0.38 Hz. Based on the WG measurements, no surface waves were present below the peak frequency, $f_p = 0.19$ Hz. Besides somewhat weaker peak spectrum level, the wave state can be considered as a well developed for $U = 6$ m/s (wave age $U/c_p \approx 0.83$).

3. Analyzed Parameters and their Relations

The instantaneous NRCS, $\sigma(t)$, and DV, $v(t)$, were computed as the 0th and 1st moments of the instantaneous spectrum, $S(f, t) = \langle |FFT(I + iQ)|^2 \rangle$, estimated using Fourier transform of raw in-phase and quadrature signals, I/Q, see e.g., [20,25,26] over consecutive $\tau = 0.2$ -s time intervals, $[t - \tau/2; t + \tau/2]$,

$$\sigma(t) = \int S(f, t) df, \quad (1)$$

$$v(t) = \pi k_r^{-1} \int f S(f, t) df / \sigma(t) \quad (2)$$

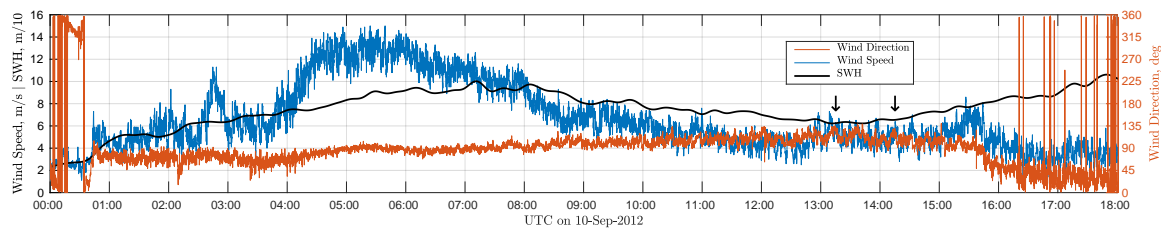


Figure 1. Wind speed, wind direction, and significant wave height (SWH) on 12-Sep-2012. Radar acquisition time span is marked by the two black arrows.

79 where $k_r = 785 \text{ rad/m}$ is the radar wavenumber.

LF variations are visualized by applying the running time mean:

$$\text{avg}(X(t)) = \int X(t')W(t' - t, \Delta)dt', \quad (3)$$

80 where $W(t, \Delta)$ is the normalized rectangular window with width, Δ .

Signal envelope, reflecting group structure, is estimated using the running variance:

$$\text{var}(X(t)) = \text{avg}([X(t) - \text{avg}(X(t))]^2) \quad (4)$$

The standard relationship between radar signal variations and wave parameters is employed [1,3]. Fourier harmonic of DV variations due to orbital velocities of resolved surface waves reads:

$$v = a\omega G, \quad (5)$$

where $a = a(\omega)$ is the Fourier harmonic of wave elevation, ω is the wave angular frequency, $G = \cos \phi \sin \theta + i \cos \theta$ is the geometric coefficient accounting for horizontal and vertical orbital velocity components, ϕ is the azimuthal angle between wave vector and radar incidence plane, θ is the incidence angle. Thus, the Doppler velocity spectrum S_{vv} , and the sea surface elevation spectrum, S_{zz} , are related as

$$S_{zz} = \omega^2 |G|^2 S_{vv}. \quad (6)$$

81 where S_{xy} stands for the cross-spectrum of x and y .

82 In terms of linear Modulation Transfer Function (MTF), NRCS variation is a linear function of
83 wave slope [1,3]. For upwind radar measurements analyzed in this paper we suppose all waves are
84 traveling towards the radar (a unidirectional sea). The NRCS can then be expressed via mean and
85 variations:

$$\sigma = \bar{\sigma} + \sigma' = \bar{\sigma}(1 + M\zeta), \quad (7)$$

86 where $\bar{\sigma}$ is the mean NRCS not disturbed by waves, $\sigma' = \sigma'(\omega)$ is the Fourier harmonic of NRCS
87 variation, $\zeta = \zeta(\omega)$ is the Fourier harmonic of wave slope with amplitude ak , k is the wavenumber
88 corresponding to ω , and $M = M(\omega)$ is the linear MTF.

The MTF can be evaluated from either WG or DV using the deep water gravity wave dispersion relationship, $\omega = \sqrt{gk}$, (applicable to our measurements):

$$M = \frac{\sigma'}{\bar{\sigma}\zeta} = \frac{gS_{z\sigma}}{\bar{\sigma}\omega^2 S_{zz}} = \frac{gGS_{v\sigma}}{\bar{\sigma}\omega S_{vv}}, \quad (8)$$

89 where g is the gravity acceleration.

90 Conversely, if the MTF is known, the NRCS time series can be reconstructed from either WG or
91 DV given $G = \sin(48^\circ) + i \cos(48^\circ)$ for the presented data. In the frequency range, $f_p < f < 0.6 \text{ Hz}$,

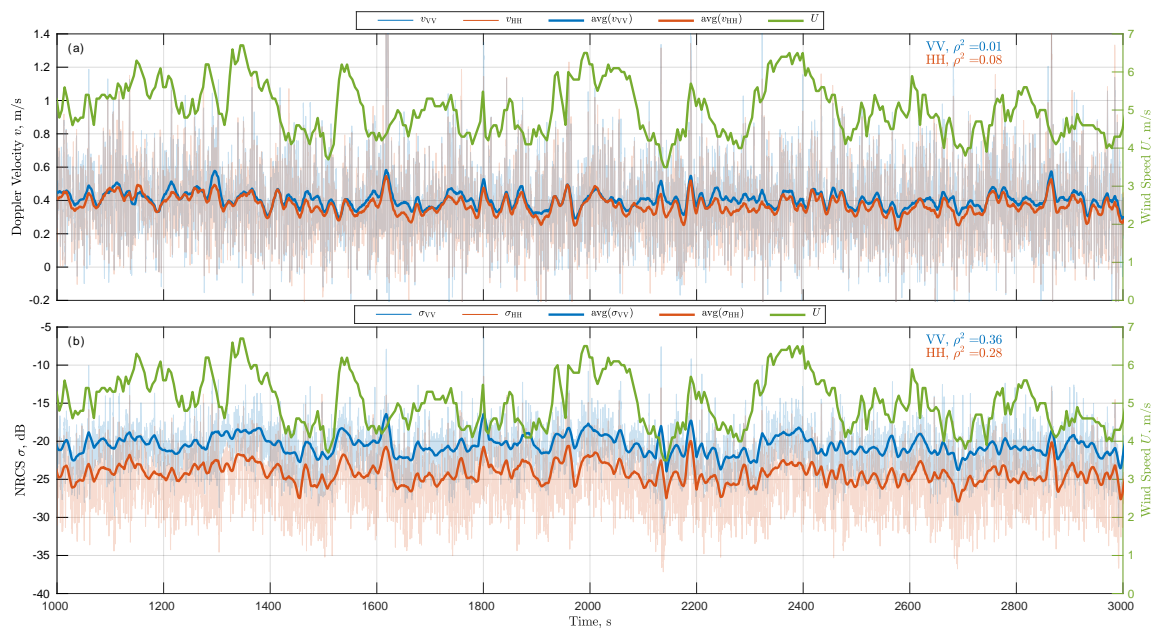


Figure 2. Time series of 10 s average (top panel) DV and (bottom panel) NRCS. Green – wind speed, bold blue/orange – VV/HH, ρ^2 is the corresponding squared correlation wind speed.

the average magnitude of linear MTF is 13.5 and 17 for VV and HH polarization, respectively. The Hilbert transform is applied to DV and WG data to estimate instantaneous magnitudes and phases. The instantaneous frequency is computed from the instantaneous phase and then averaged over $\Delta=10$ s time intervals (approximately two dominant wave periods). Eqs. (5,7) are used to retrieve instantaneous wave and radar parameters, z , ζ , v , σ assuming monochromatic sea within Δ time interval.

4. System Noise Estimation

To rule out a possibility that LF variations are instrumental artifacts, the noise introduced by the measuring system itself was estimated directly by directing the radar on a metal corner reflector spinning at 80 rpm. Each time the reflector faced the radar, it produced NRCS and DV signals, from which noise-equivalent spectra S_{vv} , $S_{\sigma\sigma}$, and $S_{v\sigma}$ were computed.

5. Observed Low-Frequency Signatures

Measured Ka-band sea surface NRCS and DV (Fig. 2) and their corresponding spectra (Fig. 3) demonstrate noticeable LF variations similar to those observed by [17,19] in the X-band.

Spectral density of DV in the LF range (Fig. 3b) is about half of the peak level (HH is slightly higher). Noise spectrum of DV (Fig. 3b) is about 4 orders of magnitude weaker and can be neglected. Conversion of DV spectrum to elevation spectrum (6) involves the ω^{-2} factor and results in unrealistic spectral behavior in the LF range (Fig. 3a).

LF part of NRCS spectrum is comparable in magnitude to the peak level (Fig. 3c) (HH is larger again). The NRCS system noise is also 4 orders of magnitude less than the NRCS signal and is disregarded.

In the LF range, the DV-NRCS cross-spectrum (Fig. 3d) is non-zero and well above the noise level indicating that LF variations of DV and NRCS are coherent. The temporal correlation between DV and NRCS is generally positive in LF ($f < f_p$) and wave ($f > f_p$) frequency ranges. The total time mean Doppler contribution integrated over the whole frequency domain $V = \overline{\sigma'v'} / \overline{\sigma} = \text{Re}\{\int S_{v\sigma} df\} / \overline{\sigma}$, contains about 30% relative contribution from the LF part.

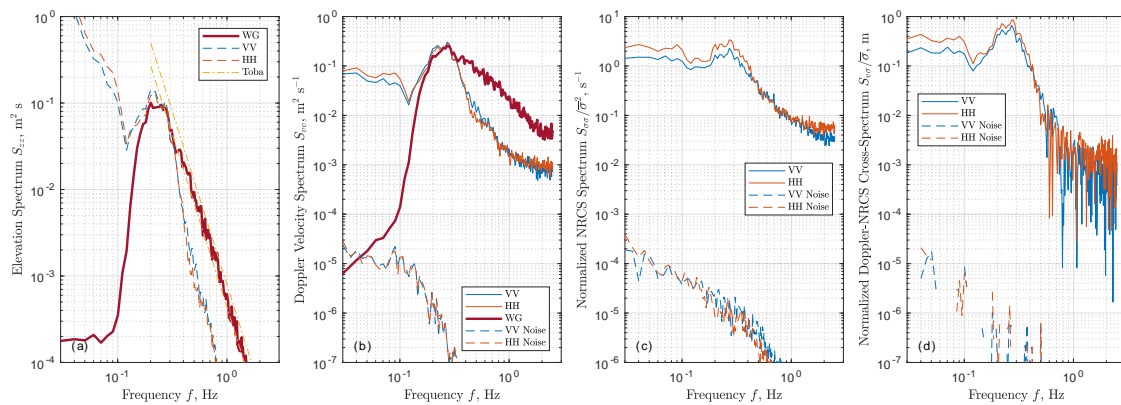


Figure 3. Spectra of (a) elevations, (b) DV, (c) NRCS, and (d) real part of DV-NRCS cross-spectrum (only positive values are shown). Dashed lines on (b,c,d) plots correspond to noise equivalent levels. Red – WG measurements, blue/orange – VV/HH polarizations. Yellow dashed lines correspond to Toba's, f^{-4} , empirical model [24].

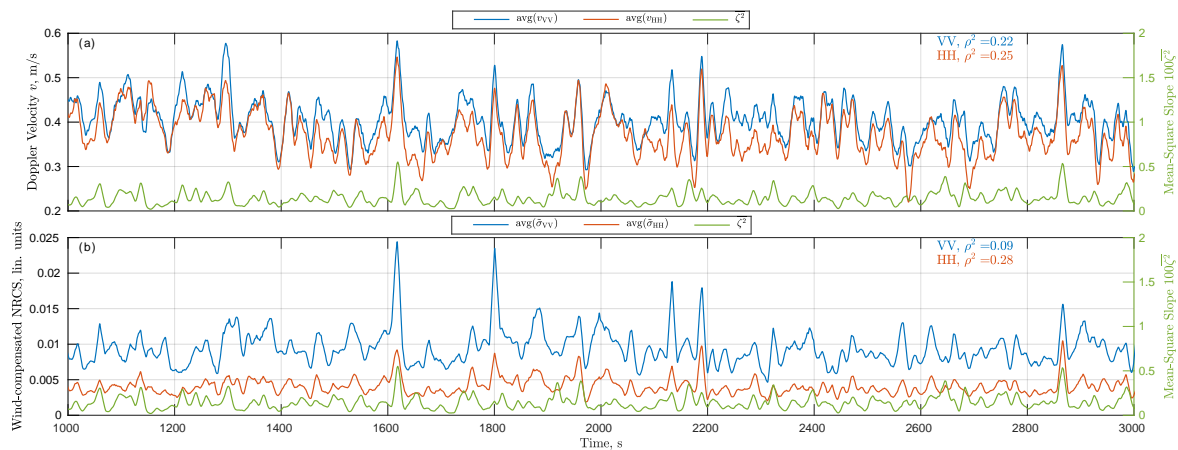


Figure 4. Time series of (top panel) DV and (bottom panel) NRCS. Green – mean-square slope, bold blue/orange – VV/HH. Average interval is 10 s.

Some of previous hypotheses of the origin of LF radar variations involve wind turbulence [17]. Comparing time series of LF DV and NRCS with LF wind speed (Fig. 2) suggests that the NRCS is correlated with wind, while the DV is not. Alternative mechanisms of the origin of LF radar variations involve wave group structure that modulates i) surface mean-square slope (MSS), which affects the LF NRCS in accordance with the two-scale model, $\sigma = \bar{\sigma}(1 + P\bar{\zeta}^2)$ [18], ii) intermediate waves to which shorter parasitic waves are bounded (LF DV mechanism, [19]), iii) wave breaking inhomogeneity [21] that imprints on sub-peak frequency variability of both DV and NRCS [20].

As a proxy for wave group, we use the running slope variance, $\text{var}(\zeta) = \bar{\zeta}^2$, estimated from radar DV. We compare this “running” MSS with average DV (Fig. 4a) and wind-compensated NRCS, i.e. NRCS from which wind-induced variations are removed, $\bar{\sigma} = \sigma - aU^n$, where the wind exponent n is set to 3 and a is determined by the linear fit, $\sigma = aU^n$ (Fig. 4b). The LF variations of DV and NRCS are related to the running mean MSS, but to a lesser extent than to the wind speed. As expected from the two-scale model e.g. [18], HH NRCS is stronger affected by MSS than VV NRCS.

Linear correlation analysis suggests that wind accounts for $\sim 30\%$ of the total LF NRCS (slower than 10 s) variance, while only 10% (30%) of the residual, non-wind-induced, variance is accounted for by MSS variations at VV (HH) polarization, respectively.

In contrast, LF DV weakly correlates with the wind, however $\sim 20\%$ of its variance is explained by MSS variations. Notice, that the correlation between DV and MSS is also affected by the fact that the MSS is retrieved from the DV itself (WG data are not used because they were measured far from the radar footprint). DV-based MSS proxy accounts only for waves longer than the radar footprint length that don't respond to immediate wind fluctuations, which in turn explains rather low correlation between MSS and wind.

6. Non-Linear Transfer Function

A non-zero correlation between MSS and LF NRCS reflects a non-linearity of NRCS-wave slope transfer. In general, a non-linear transfer results in spectrum broadening by leaking energy into multiple order harmonics and sub-harmonics [27,28]. Our focus is on the latter as a potential cause of observed LF features in both NRCS and DV.

The impact of non-linearity is demonstrated by the shape of NRCS probability density function (PDF, Fig. 5a,b) that is strongly skewed and has a non-Gaussian shape. If a linear MTF is used to retrieve the NRCS from observed wave slopes, which have quasi-Gaussian PDF, the PDF of retrieved NRCS is obviously quasi-Gaussian, in contrast with the observed PDF.

Because the characteristic magnitude of the linear MTF is significant ($\approx 10 - 20$), even small wave slopes produce NRCS variations comparable in magnitude to the NRCS itself. As an alternative, a non-Linear MTF (NLMTF) can be used [29,30]

$$\sigma = \sigma_0 \exp(M\zeta), \quad (9)$$

to which the traditional linear MTF (7) is the first order approximation.

For the normally distributed slopes ζ , the NRCS given by eq. (9) is log-normally distributed:

$$p(\sigma) = p(\sigma(\zeta)) \left| \frac{d\zeta}{d\sigma} \right| = \frac{1}{\sqrt{2\pi\zeta^2 M\sigma}} \exp \left\{ -\frac{\log^2(\sigma/\sigma_0)}{2M^2\zeta^2} \right\}. \quad (10)$$

Since the "non-linear" NRCS is non-Gaussian, the σ_0 -parameter is not the mean NRCS, $\bar{\sigma}$, but they are related:

$$\sigma_0 = \bar{\sigma} \exp \left\{ -\frac{M^2\zeta^2}{2} \right\}. \quad (11)$$

The PDF of observed NRCS is approximated well by a log-normal distribution eq. (10) as shown in Figs. 5a,b. Observed NRCS spectra and DV-NRCS cross-spectra are also reproduced well using the NLMTF (Fig. 6). As expected, the linear MTF doesn't produce LF components if applied to WG data. Switching to NLMTF makes LF spectral level non-zero but still lower than in observations. LF components are produced if the DV is used as a wave probe and the linear MTF is applied. Indeed, it reflects the presence of LF components in measured DV. Finally, if DV-based wave elevations are non-linearly transformed into the NRCS, the simulated co- and cross-spectra have well pronounced LF features.

The difference between measured and wind-compensated NRCS spectra is small suggesting that near surface and anemometer height wind variations are not well correlated at $0.01 \text{ Hz} < f < 0.1 \text{ Hz}$. Our wind detection setup was primarily designed to control the background atmospheric conditions, i.e. record-mean wind velocity. The measurement height (21-m height) as well as wind vane anemometer sampling rate (0.2 Hz) both are not optimal to detect $0.01 - 0.1 \text{ Hz}$ wind fluctuations, which may be associated with the atmospheric boundary layer perturbations produced by wave groups confined to lower heights, which are simply missed by 21-m height sensor. Due to the above wind detection limitations, it might be not surprising to see such weak impacts of observed wind fluctuations on NRCS spectra in the LF range (Fig. 6).

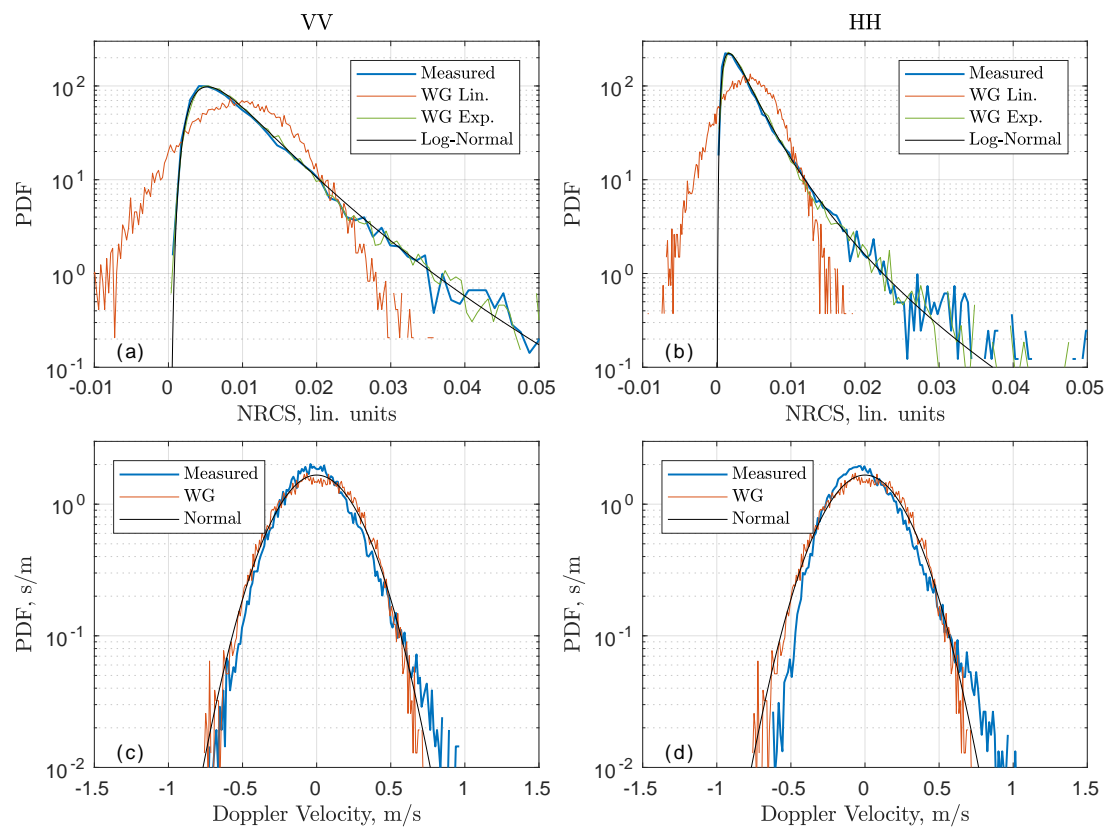


Figure 5. Probability density function (PDF) of (a,b) NRCS and (c,d) DV for (a,c) VV polarization and (b,d) HH polarization. Blue – measurements, orange – retrieved using linear MTF (7), green – retrieved using non-linear MTF (9), black – theoretical curve (log-normal for NRCS, normal for DV).

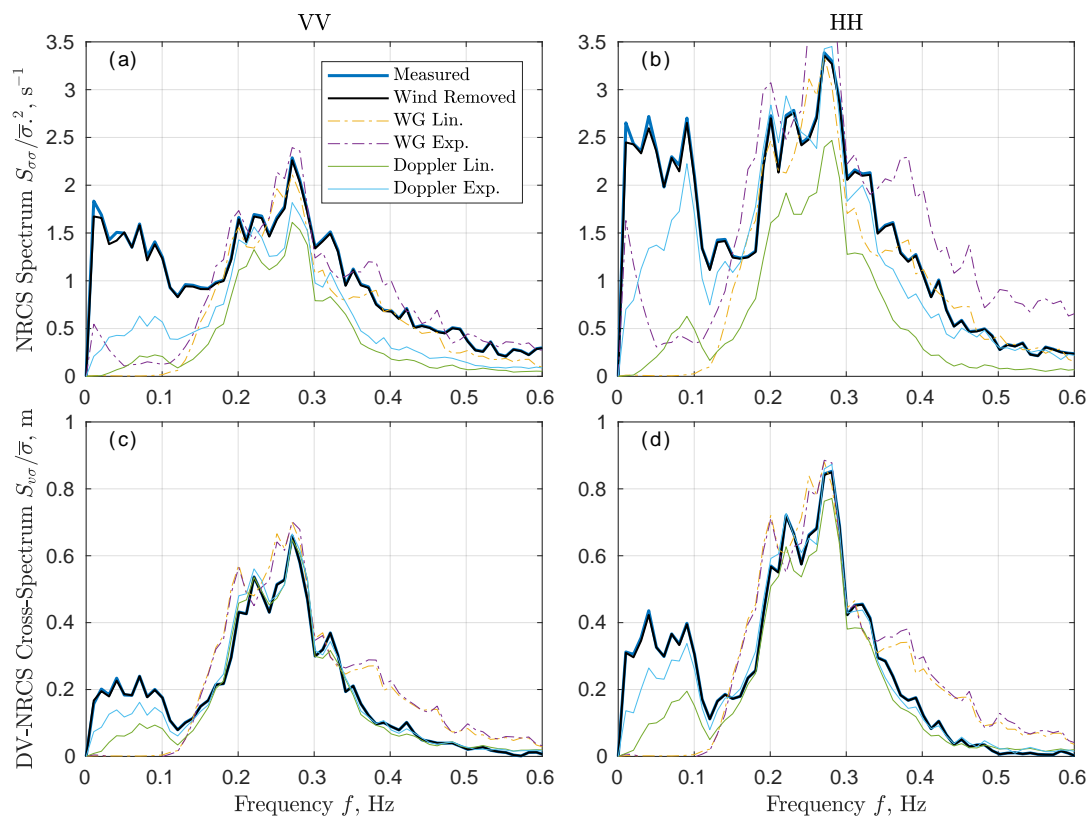


Figure 6. Measurements and various estimates of (a,b) NRCS spectra and (c,d) DV-NRCS spectra for (a,c) VV polarization and (b,d) HH polarization.

On the other hand, the DV PDF is quasi-Gaussian (Fig. 5c,d) indicating that measured DV is reproduced well by WG data using the linear MTF (with the exception of HH polarization for which the PDF is a slightly skewed). Hence, LF DV variations cannot be explained by the NLMTF. However, the DV measured by a radar is footprint-averaged local DV weighted by local NRCS. Because the local NRCS is a non-linear function of local wave slopes, the measured DV is affected by non-linearity of NRCS transfer function. In other words, the observed LF DV signatures can result from NRCS non-linearity that is involved through the footprint averaging.

It is also surprising that DV-based surface elevation works better than in-situ WG data for radar spectra estimates (Fig. 5). This fact may be related to distortions of apparent frequency of shorter waves by orbital velocity of longer waves, in turn suggesting that WG-based frequency attribution of wave elevation is not reliable at high frequencies. Next we will perform a numerical simulation to overcome a lack of information on unresolved short waves.

7. Numerical Simulation

To model one-dimensional moving surface, a semi-empirical wavenumber KMC spectrum [31,32] is used. The length of simulated domain is 400 m (≈ 10 dominant wavelengths). Spatial resolution 0.05 m corresponds to the shortest wavelength. The initial surface is a superposition of harmonics with amplitudes obeying the KMC spectrum and phases randomly distributed over $[0; 2\pi]$ interval. The phase speed of each harmonic is determined by the dispersion relation, $c = \sqrt{g/k + \gamma k}$, where $\gamma = 7.3 \times 10^{-5}$ N/m is the surface tension. All harmonics propagate towards an upwind looking radar oriented at $\theta = 48^\circ$ incidence angle. Simulation lasts for 12 hours (about 10000 dominant wave periods) with 0.1 s time step.

The local NRCS is computed using NLMTF from the local surface slope (gradient), while the local DV is a sum of orbital velocities of all harmonics. The radar NRCS and DV are footprint averages:

$$\sigma(t) = \int \sigma(x,t)W(x)dx / \int W(x)dx \quad (12)$$

$$v(t) = \int v(x,t)\sigma(x,t)W(x)dx / \int \sigma(x,t)W(x)dx \quad (13)$$

where $W(x)$ is the Gaussian-shaped two-way antenna pattern. We will explore different values of $W(x)$ half-width, including 4m width that corresponds to our radar footprint.

Simulated DV and NRCS spectra, and their cross-spectra are shown in Fig. 7 along with measurements. Given rather simple 1-D surface elevation model, the overall consistency between measurements and simulations is remarkably good. The simulated DV peak level is higher than in observations because all wave energy is directed into a single direction, while the real spectrum is not unidirectional. The simulation nicely reproduces the LF signatures for all spectra with the exception of VV NRCS (Fig. 7a). This can be explained by the presence of LF wind variability (not accounted for by this simple 1-D model) to which VV NRCS is more sensitive due to higher contribution of Bragg backscattering. VV cross-spectrum (Fig. 7a) is reproduced better than NRCS spectrum indicating that wind-induced variability is important for NRCS and to much lesser extent for DV.

Although the hydrodynamics MTF responsible for short-long wave correlation is not directly included in the simulation, its impact on LF variations is partially present through the using of observed MTF magnitude ($M = 12 - 16$), which otherwise would be lower for the tilting only.

8. The Role of Non-Linearity

The simulated 1-D surface is used to evaluate the importance of non-linear radar imaging effects. First, we test how good the linear MTF approximation (7) is, if the actual transfer function is non-linear (9). The DV and NRCS are simulated using the NLMTF with the magnitude varying from 1 to 40. Footprint half-width $W(x)$ in (12, 13) is set to 1 m to increase the footprint cut-off frequency of simulated spectra. Based on simulated NRCS and DV, the linear MTF is estimated using (8).

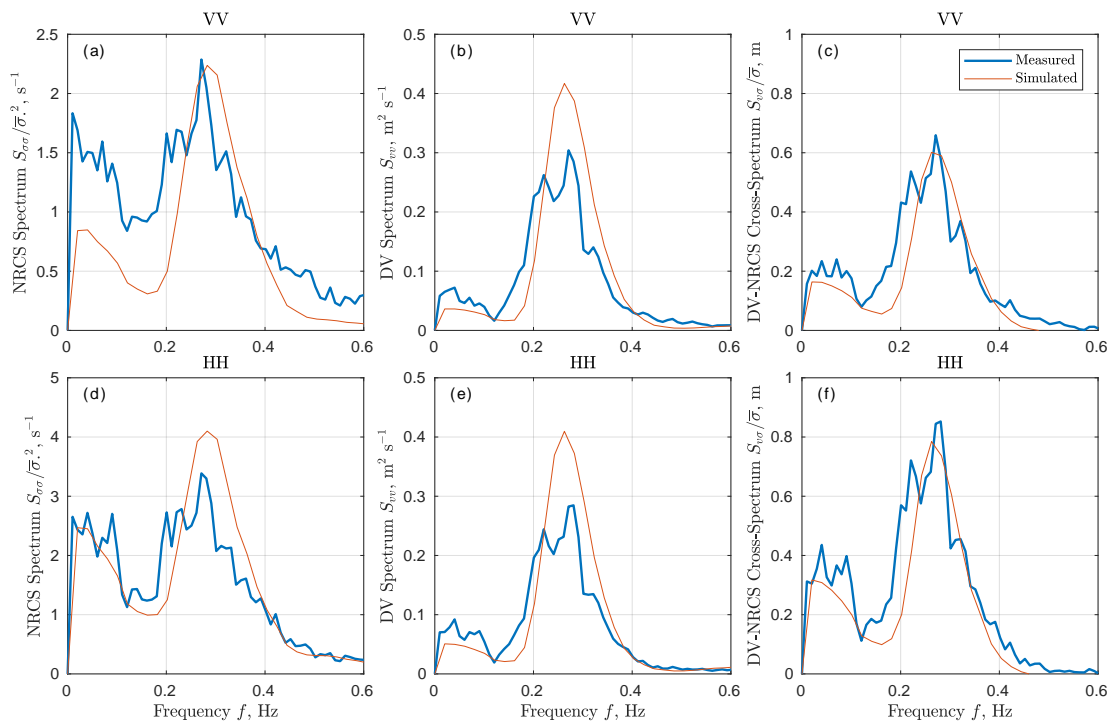


Figure 7. Simulated and measured (a,d) NRCS, (b,e) DV, (c,f) DV-NRCS spectra for (top row) VV polarization and (bottom row) HH polarization.

The estimated magnitude of linear MTF (Fig. 8a) equals the original MTF magnitude, $|M|$, for $f_p < f < f_1$ with the upper frequency, f_1 , determined by the footprint size. The linear MTF estimate level averaged over $[0.2; 0.6]$ Hz frequency interval is close (to within 10% error corridor) to the original MTF magnitude for $M < 20$ (Fig. 8b, blue symbols), although its uncertainty increases at higher $|M|$.

The time mean DV, or the DV averaged over the whole wave spectrum, is also estimated from linear MTF and known wave spectrum using (5,7):

$$V = \overline{v\sigma} / \overline{\sigma} = g^{-1} \text{Re}\{G^* M \int \omega^3 S_{zz}(\omega) d\omega\} = g^{1/2} \text{Re}\{G^* M \int k^{3/2} S_{zz}(k) dk\} \quad (14)$$

The ratio of DV estimate ($\overline{v\sigma} / \overline{\sigma}$) based on linear MTF (14) to DV estimate based on non-linear MTF (13) is close to 1 for $|M| < 20$ to within 10% error (Fig. 8b). For the majority of practical cases (excluding near-threshold winds and large θ with $M > 20$ [23]), the impact of non-linear effects on radar DV can be ignored. One simplification made for DV estimation (14) is the using of frequency independent MTF, which is not the case for swell that has higher MTF due to wave-induced wind variations [2,33], which are not included in our simple simulations. Thus our numerical simulations suggest that linear MTF (7) is a good approximation for non-linear MTF (9) given small long wave slopes.

9. Summary

This study presents the analysis of LF variations of Doppler radar backscattering from the sea surface based on a Ka-band field measurements. They are separated by applying the running 10-s mean roughly corresponding to double period of dominant waves. A specialized laboratory experiment was conducted to estimate the measuring system noise and to prove that it is not the cause of observed LF variations. LF winds explain about $\sim 30\%$ of LF NRCS variance, while LF DV does not correlate with LF winds. Non-wind-induced NRCS is partly explained by LF mean-square slope (10% / 30% for VV / HH polarization, respectively) indicating non-linear transfer between slopes and NRCS.

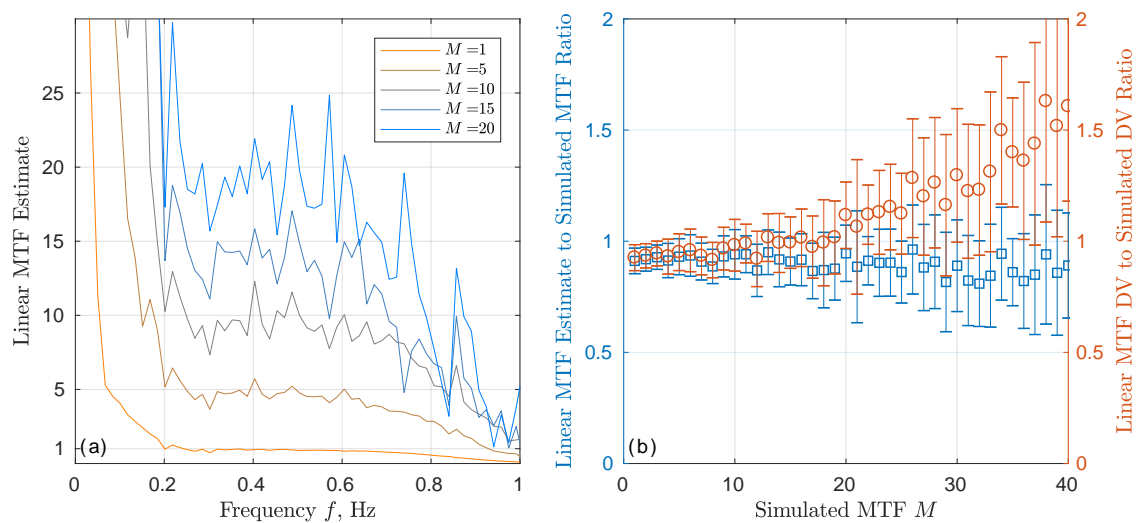


Figure 8. (a) Linear MTF estimated using (8) based on non-linearly simulated NRCS for various M in (9). (b) Ratio of linear MTF estimate (8) averaged at $0.2 \text{ Hz} < f < 0.6 \text{ Hz}$ to M (left y-axis) and ratio of DV estimate based on linear MTF (14) to DV simulated using non-linear MTF (13, right y-axis).

As deduced from the sample distribution analysis, the local NRCS is essentially a non-linear function of wave slopes in line with previous studies [27–30]. This non-linearity explains observed NRCS spectra, including their LF part, if non-linear MTF is applied to wave slopes estimated from instantaneous radar DV (orbital velocity). The DV has quasi-Gaussian distribution (positive tails are caused by wave breaking) indicating that it is a linear function of surface slopes. Hence, LF variations in radar DV is a consequence of spatial averaging that is a product of the local DV weighted by the local non-linear NRCS.

Impact of nonlinearity of radar measurements is tested using a 1-D surface elevation simulation based on the semi-empirical wave spectrum [31] corresponding to observed wind and wave fetch. If the NRCS is modeled using a non-linear transfer function, the measured DV and NRCS spectra are adequately reproduced by the simulation even though the hydrodynamics effects are not included. Simulated LF variance of VV NRCS is underestimated by a factor of ≈ 2 suggesting that wind variability, which is not included in the simulation, is still important. However, the DV-NRCS cross-spectrum is simulated well even without the inclusion of wind variability effect. This suggests that LF DV is not strongly affected by LF winds, which impact can be ignored for the time mean DV.

The relationship between the LF radar variation and the non-linearity of modulation transfer function may explain other available observations. In particular, the magnitude of LF variations in the L-band are almost twice as large as in the X-band [17]. This is explained by larger L-band MTF magnitude (e.g. see Fig. 11 in [34]) that results in more pronounced nonlinearity. The increase of LF level of DV spectra at large incidence angles [19,20] is explained by larger radar footprint size and by larger MTF magnitude caused by hydrodynamics modulation of wedge scattering.

Simulations with different MTF magnitudes show that MTF nonlinearity has little effect on estimated linear MTF as well as on estimated time mean DV. This confirms that traditional linear MTF [1,3] is a good approximation for real non-linear radar MTF, while LF signatures are “artifacts” caused by MTF nonlinearity and spatial averaging over finite radar footprint.

Acknowledgments: The core support of the work was provided by Russian Science Foundation grant No. 17-77-10052. Field experiments were supported by FASO of Russia under the State Assignment (No. 0827-2018-0002). Sea surface simulation was supported by the Ministry of Science and Education (Goszadanie 5.2928.2017/PP) and NASA/PhO. The authors would like to thank Anton Garmashov of MHI for providing standard meteorological measurements.

Author Contributions: V.K. and Yu.Yu. conceived and designed the experiments; V.K., B.C. and S.G. provided sea surface model for numerical simulations; Yu.Yu. performed the experiments, analyzed the data, and wrote the paper.

Conflicts of Interest: The authors declare no conflict of interest.

Abbreviations

The following abbreviations are used in this manuscript:

DV	Doppler Velocity
FFT	Fast Fourier Transform
HH	Horizontal Transmit-Receive Polarization
LF	Low Frequency
MSS	Mean-Square Slope
MTF	Modulation Transfer Function
NLMTF	Non-Linear Modulation Transfer Function
NRCS	Normalized Radar Cross-Section
PDF	Probability Density Function
VV	Vertical Transmit-Receive Polarization
UTC	Coordinated Universal Time
WG	Wave Gauge

- Keller, W.C.; Wright, J.W. Microwave scattering and the straining of wind-generated waves. *Radio Science* **1975**, *10*, 139–147. doi:10.1029/RS010i002p00139.
- Schröter, J.; Feindt, F.; Alpers, W.; Keller, W.C. Measurement of the ocean wave-radar modulation transfer function at 4.3 GHz. *J. Geophys. Res. (Oceans)* **1986**, *91*, 923–932. doi:10.1029/JC091iC01p00923.
- Plant, W.J. The Modulation Transfer Function: Concept and Applications. *Radar Scattering from Modulated Wind Waves* **1989**, pp. 155–172.
- Goldstein, R.M.; Zebker, H.A. Interferometric radar measurement of ocean surface currents. *Nature* **1987**, *328*, 707–709. doi:10.1038/328707a0.
- Romeiser, R.; Thompson, D.R. Numerical study on the along-track interferometric radar imaging mechanism of oceanic surface currents. *IEEE Trans. Geosci. Remote Sens.* **2000**, *38*, 446–458. doi:10.1109/36.823940.
- Martin, A.; Gommenginger, C. Towards wide-swath high-resolution mapping of total ocean surface current vectors from space: Airborne proof-of-concept and validation. *Remote Sensing of Environment* **2017**, *197*, 58–71. doi:http://dx.doi.org/10.1016/j.rse.2017.05.020.
- Chapron, B.; Collard, F.; Ardhuin, F. Direct measurements of ocean surface velocity from space: Interpretation and validation. *J. Geophys. Res. (Oceans)* **2005**, *110*, 7008. doi:10.1029/2004JC002809.
- Johannessen, J.A.; Chapron, B.; Collard, F.; Kudryavtsev, V.; Mouche, A.; Akimov, D.; Dagestad, K.F. Direct ocean surface velocity measurements from space: Improved quantitative interpretation of Envisat ASAR observations. *Geophys. Res. Lett.* **2008**, *35*, 22608. doi:10.1029/2008GL035709.
- Mouche, A.A.; Collard, F.; Chapron, B.; Dagestad, K.F.; Guitton, G.; Johannessen, J.A.; Kerbaol, V.; Hansen, M.W. On the Use of Doppler Shift for Sea Surface Wind Retrieval From SAR. *IEEE Trans. Geosci. Remote Sens.* **2012**, *50*, 2901–2909. doi:10.1109/TGRS.2011.2174998.
- Bourassa, M.A.; Rodriguez, E.; Chelton, D. Winds and currents mission: Ability to observe mesoscale AIR/SEA coupling. *Proc. Int. Geosci. Remote Sens. Symp.*, 2016, pp. 7392–7395. doi:10.1109/IGARSS.2016.7730928.
- Ardhuin, F.; Aksenov, Y.; Benetazzo, A.; Bertino, L.; Brandt, P.; Caubet, E.; Chapron, B.; Collard, F.; Cravatte, S.; Dias, F.; Dibarboure, G.; Gaultier, L.; Johannessen, J.; Korosov, A.; Manucharyan, G.; Menemenlis, D.; Menendez, M.; Monnier, G.; Mouche, A.; Noguier, F.; Nurser, G.; Rampal, P.; Reniers, A.; Rodriguez, E.; Stopa, J.; Tison, C.; Tissier, M.; Ubelmann, C.; van Seville, E.; Vialard, J.; Xie, J. Measuring currents, ice drift, and waves from space: the Sea Surface KInematics Multiscale monitoring (SKIM) concept. *Ocean Science Discussions* **2017**, *2017*, 1–26. doi:10.5194/os-2017-65.

12. Bao, Q.; Lin, M.; Zhang, Y.; Dong, X.; Lang, S.; Gong, P. Ocean Surface Current Inversion Method for a Doppler Scatterometer. *IEEE Trans. Geosci. Remote Sens.* **2017**, *55*, 6505–6516. doi:10.1109/TGRS.2017.2728824.
13. Rodriguez, E.; Wineteer, A.; Perkovic-Martin, D.; Gál, T.; Stiles, B.; Niamsuwan, N.; Rodriguez Monje, R. Estimating Ocean Vector Winds and Currents Using a Ka-Band Pencil-Beam Doppler Scatterometer. *Remote Sens.* **2018**, *10*(4), 576. doi:10.3390/rs10040576.
14. Nouguier, F.; Chapron, B.; Collard, F.; Mouche, A.; Rascle, N.; Ardhuin, F.; Wu, X. Sea Surface Kinematics From Near-Nadir Radar Measurement. *IEEE Trans. Geosci. Remote Sens.* **2018**. accepted.
15. Fois, F.; Hoogeboom, P.; Le Chevalier, F.; Stoffelen, A. An analytical model for the description of the full-polarimetric sea surface Doppler signature. *J. Geophys. Res. (Oceans)* **2015**, *120*, 988–1015. doi:10.1002/2014JC010589.
16. Yurovsky, Y.Y.; Kudryavtsev, V.; Grodsky, S.A.; Chapron, B. Normalized Radar Backscattering Cross-section and Doppler Shifts of the Sea Surface in Ka-band. 2017 Progress in Electromagnetic Research Symposium (PIERS); , 2017. in press.
17. Plant, W.J.; Keller, W.C.; Cross, A. Parametric dependence of ocean wave-radar modulation transfer functions. *J. Geophys. Res. (Oceans)* **1983**, *88*, 9747–9756. doi:10.1029/JC088iC14p09747.
18. Grodsky, S.A.; Kudryavtsev, V.N.; Bol'shakov, A.N.; Smolov, V.E. Experimental investigation of fluctuations of radar signals caused by surface waves. *Physical Oceanography* **2001**, *11*, 333–352. doi:10.1007/BF02509228.
19. Plant, W.J. A model for microwave Doppler sea return at high incidence angles: Bragg scattering from bound, tilted waves. *J. Geophys. Res. (Oceans)* **1997**, *102*, 21131–21146. doi:10.1029/97JC01225.
20. Hwang, P.A.; Sletten, M.A.; Toporkov, J.V. A note on Doppler processing of coherent radar backscatter from the water surface: With application to ocean surface wave measurements. *J. Geophys. Res. (Oceans)* **2010**, *115*, n/a–n/a. C03026, doi:10.1029/2009JC005870.
21. Donelan, M.; Longuet-Higgins, M.S.; Turner, J.S. Periodicity in whitecaps. *Nature* **1972**, *239*, 449–451. doi:10.1038/239449a0.
22. Yurovsky, Y.Y.; Kudryavtsev, V.N.; Grodsky, S.A.; Chapron, B. Ka-Band Dual Copolarized Empirical Model for the Sea Surface Radar Cross Section. *IEEE Trans. Geosci. Remote Sens.* **2017**, *55*, 1629–1647. doi:10.1109/TGRS.2016.2628640.
23. Yurovsky, Y.Y.; Kudryavtsev, V.N.; Chapron, B.; Grodsky, S.A. Modulation of Ka-band Doppler Radar Signals Backscattered from the Sea Surface. *IEEE Trans. Geosci. Remote Sens.* **2018**, pp. 1–19. in press, doi:10.1109/TGRS.2017.2787459.
24. Toba, Y.; Koga, M. A parameter describing overall conditions of wave breaking, whitecapping, sea-spray production and wind stress. In *Oceanic Whitecaps*; Monahan, E.C.; Niocaill, G.M., Eds.; Reidel Publishing Company, 1986; pp. 37–47.
25. Jessup, A.T.; Melville, W.K.; Keller, W.C. Breaking waves affecting microwave backscatter 1. Detection and verification. *J. Geophys. Res. (Oceans)* **1991**, *96*, 20547–20559. doi:10.1029/91JC01993.
26. Thompson, D.R.; Jensen, J.R. Synthetic aperture radar interferometry applied to ship-generated internal waves in the 1989 Loch Linnhe experiment. *J. Geophys. Res. (Oceans)* **1993**, *98*, 10259–10270.
27. Hesany, V.; Moore, R.K.; Gogineni, S.P.; Holtzman, J.C. Slope-induced nonlinearities on imaging of ocean waves. *IEEE J. Oceanic Eng.* **1991**, *16*, 279–284. doi:10.1109/48.90884.
28. Schmidt, A.; Bao, M. The modulation of radar backscatter by long ocean waves: A quadratically nonlinear process? *J. Geophys. Res. (Oceans)* **1998**, *103*, 5551–5562. doi:10.1029/97JC00634.
29. Trunk, G.V. Radar Properties of Non-Rayleigh Sea Clutter. *IEEE Transactions on Aerospace and Electronic Systems* **1972**, *AES-8*, 196–204. doi:10.1109/TAES.1972.309490.
30. Gotwols, B.L.; Thompson, D.R. Ocean microwave backscatter distributions. *J. Geophys. Res. (Oceans)*, *99*, 9741–9750. doi:10.1029/93JC02649.
31. Kudryavtsev, V.N.; Makin, V.K.; Chapron, B. Coupled sea surface-atmosphere model: 2. Spectrum of short wind waves. *J. Geophys. Res. (Oceans)* **1999**, *104*, 7625–7639. doi:10.1029/1999JC900005.
32. Yurovskaya, M.V.; Dulov, V.A.; Chapron, B.; Kudryavtsev, V.N. Directional short wind wave spectra derived from the sea surface photography. *J. Geophys. Res. (Oceans)* **2013**, *118*, 4380–4394. doi:10.1002/jgrc.20296.
33. Alpers, W.; Ross, D.; Rufenach, C. On the detectability of ocean surface waves by real and synthetic aperture radar. *J. Geophys. Res. (Oceans)* **1981**, *86*, 6481–6498.

351 34. Feindt, F.; Schroeter, J.; Alpers, W. Measurement of the ocean wave-radar modulation transfer function
352 at 35 GHz from a sea-based platform in the North Sea. *J. Geophys. Res. (Oceans)* **1986**, *91*, 9701–9708.
353 doi:10.1029/JC091iC08p09701.